Nano Research

Open Access

Research Article

Multifunctional nanoparticle-reinforced tissue-derived hydrogel for accelerated healing of drug-resistant *Pseudomonas aeruginosa* infected wounds

Jialu Lang[1,2,3,§], Chunlei Shan[1,§], Yuanzhi Ju[2], Qi Zhu[3], Jiawen Zhu[3], Xiaochuan Wu[3], Jiahao Hu[3], Yuanyan Huang[3], Di Chen[2], Gang Han[1] ✉, Yongzhong Du[2,3] ✉, and Zhenwei Yu[1,2] ✉

[1] *Department of Pharmacy, Sir Run Run Shaw Hospital, School of Medicine, Zhejiang University, Hangzhou 310016, China*
[2] *Research Center for Clinical Pharmacy, College of Pharmaceutical Sciences, Zhejiang University, Hangzhou 310058, China*
[3] *State Key Laboratory of Advanced Drug Delivery and Release Systems, Institute of Pharmaceutics, College of Pharmaceutical Sciences, Zhejiang University, Hangzhou 310058, China*
§ *Jialu Lang and Chunlei Shan contributed equally to this work.*

Cite this article: *Nano Research*, **2026**, *19*, 94908546. https://doi.org/10.26599/NR.2026.94908546

ABSTRACT: Chronic wounds complicated by multidrug-resistant bacterial infections pose a serious therapeutic challenge. Here, we develop a multifunctional hydrogel (PmB/Ag-PDA@ECM) by integrating silver nanoparticle-modified polydopamine (Ag-PDA) and polymyxin B (PmB) into a thermosensitive, pro-regenerative extracellular matrix (ECM) hydrogel. The hydrogel exhibits favorable physicochemical properties, including a porous microstructure (49.24% porosity), rapid swelling (~ 1068%), and strong tissue adhesion (6.24 kPa). Upon near-infrared (NIR) irradiation, it achieves mild photothermal heating (~ 50 °C), triggering synergistic antibacterial effects that completely eradicate polymyxin B-resistant *Pseudomonas aeruginosa* (PRPA). *In vitro*, the hydrogel promotes keratinocyte and endothelial cell proliferation and migration, while maintaining excellent cytocompatibility and hemocompatibility. In a PRPA-infected full-thickness wound model, the hydrogel rapidly sterilizes the wound bed and accelerates wound closure. Moreover, it effectively suppresses inflammation (reduced tumor necrosis factor-alpha (TNF-α), interleukin-6 (IL-6)), promotes M2 macrophage polarization, and facilitates tissue remodeling, including neovascularization and regeneration of skin appendages. This work presents a clinically translatable hydrogel platform that simultaneously addresses antimicrobial resistance and supports high-quality tissue regeneration, offering a promising strategy for the treatment of complex infected wounds.

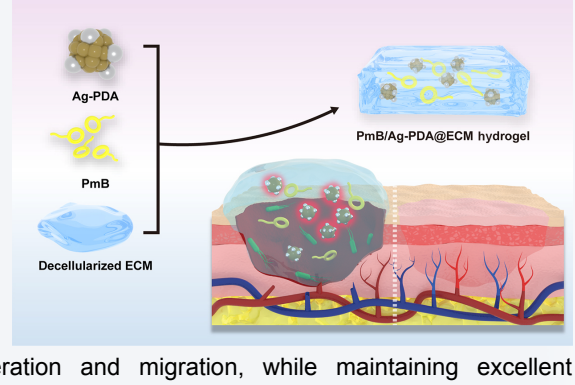

KEYWORDS: extracellular matrix hydrogel, silver-decorated polydopamine, antibiotic resistance, wound healing, photothermal therapy

1 Introduction

Chronic wounds colonized by pathogenic bacteria represent a significant and escalating threat to global public health, imposing a substantial economic burden on healthcare systems [1]. In the absence of the skin as an innate defense system, the wound bed provides a fertile environment for bacterial colonization, biofilm formation, and persistent infection [2]. Among the diverse pathogens implicated in chronic wound infections, *Pseudomonas aeruginosa* (*P. aeruginosa*) is one of the most prevalent and clinically challenging, with prevalence rates reaching up to 21% in Asia [3–5]. This opportunistic Gram-negative bacterium is notorious for establishing recalcitrant infections that impede wound healing, a characteristic largely attributed to its high intrinsic antibiotic resistance and robust biofilm-forming capability [6]. Alarmingly, *P. aeruginosa* has demonstrated increasing resistance to frontline antimicrobials, including third-generation cephalosporins and, in certain instances, to last-line agents such as polymyxin B

Received: December 18, 2025; **Revised:** February 4, 2026
Accepted: February 6, 2026

✉Address correspondence to Gang Han, 3199022@zju.edu.cn; Yongzhong Du, duyongzhong@zju.edu.cn; Zhenwei Yu, yzw_srrsh@zju.edu.cn

(PmB) [7, 8]. These developments pose a remarkable obstacle to effective treatment and underscore the urgent need for alternative therapeutic strategies capable of both eradicating resistant pathogens and promoting tissue regeneration.

Conventional wound dressings, such as cotton gauze and bandages, serve primarily as passive barriers without therapeutic efficacy required to address the complex pathophysiology of infected wounds [9, 10]. While contemporary treatments, including systemic antibiotics [11], collagen-based dressings [12], growth factors like epidermal growth factor (EGF) [13], and stem cell therapies [14], have been explored, they remain largely monofunctional and insufficient to address the critical challenge of antimicrobial resistance. To combat drug-resistant bacteria, advanced therapeutic modalities such as chemodynamic therapy (CDT) [15], photodynamic therapy (PDT) [16, 17], sonodynamic therapy (SDT) [18, 19], and photothermal therapy (PTT) [20–22] have garnered considerable attention. Among these, PTT is particularly advantageous, distinguished by its minimal side effects, high spatiotemporal controllability, low invasiveness, and a reduced propensity for inducing microbial resistance [23]. Advanced wound dressings, particularly multifunctional hydrogels, have emerged as a promising platform for integrating such therapeutic modalities [24]. With their intrinsically high water content, three-dimensional porous architecture, and excellent biocompatibility, hydrogels are considered ideal scaffolds [25]. By tailoring both their matrix structure and incorporated agents, hydrogels can be endowed with a suite of functions, including antimicrobial, anti-inflammatory, hemostatic, and sustained-release properties [24, 26]. However, many existing hydrogel systems are hampered by critical deficiencies, such as poor mechanical robustness and insufficient antimicrobial efficacy against highly resistant strains, thereby restricting their clinical applicability and effectiveness.

Herein, we report the design of a multifunctional hydrogel (designated as PmB/Ag-PDA@ECM) aimed at treating wounds infected by polymyxin B-resistant *P. aeruginosa* (PRPA) (Scheme 1). This therapeutic scaffold is constructed from a decellularized extracellular matrix (ECM) hydrogel integrated with polymyxin B and silver nanoparticle-coated polydopamine (Ag-PDA) nanostructures. The myocardial-derived ECM hydrogel provides a native-like microenvironment rich in collagen, glycosaminoglycans, and proteoglycans [27, 28]. Its biomimetic, porous 3D structure and inherent biocompatibility are designed to promote essential cellular processes, including proliferation, migration, and differentiation, thereby facilitating tissue regeneration [29]. Crucially, porcine myocardium was selected as the ECM source due to its high batch-to-batch consistency and superior hydrogel-forming capacity [30, 31]. Unlike other tissues, porcine myocardial ECM has demonstrated clinical safety in human trials for cardiac repair, underscoring its significant translational potential [32]. Moreover, its unique ability to orchestrate angiogenesis and modulate macrophage polarization toward a pro-healing (M2) phenotype makes it an ideal substrate for accelerating the repair of complex, infected cutaneous wounds [32, 33]. The incorporation of polydopamine (PDA), a bioinspired polymer, considerably enhances the mechanical robustness and tissue adhesiveness of the hydrogel [34]. Furthermore, PDA functions as a stable and efficient photothermal agent, enabling potent, broad-spectrum bactericidal activity upon near-infrared (NIR) light irradiation, facilitating deep tissue penetration [35]. The synergistic integration of silver nanoparticles (AgNPs) with PDA is a key design feature. The PDA shell not only mitigates the potential cytotoxicity of AgNPs by reducing reactive oxygen species (ROS) production and downregulating inflammatory cytokines [36, 37], but also enhances the overall photothermal efficacy by preventing AgNP aggregation and increasing NIR absorbance [38]. This synergy results in a potent combined antimicrobial action against PRPA. Critically, we implemented mild PTT (mPTT, ~ 50 °C) to circumvent the collateral damage to healthy tissue caused by conventional high-temperature PTT (> 60 °C), which often causes collateral damage to healthy tissue [39]. Instead, we implement an mPTT approach at a physiologically safer temperature (~ 50 °C) [38, 39]. At this temperature, the photothermal effect acts in concert with the membrane-disrupting activities of released Ag^+ ions and PmB, eliciting a robust tripartite antimicrobial synergy that overcomes the formidable resistance of *P. aeruginosa*. The PmB/Ag-PDA@ECM hydrogel is anticipated to effectively eradicate PRPA infection *in vivo* while simultaneously accelerating the closure and healing of complex infected wounds, which provides an emerging clinical option for chronic wounds colonized by pathogenic bacteria. This synergy results in a potent combined antimicrobial action against PRPA. Critically, we implemented mild PTT (mPTT, ~ 50 °C) to circumvent the collateral damage to healthy tissue caused by conventional high-temperature PTT (> 60 °C), which often causes collateral damage to healthy tissue [39]. Instead, we implement an mPTT approach at a physiologically safer temperature (~ 50 °C) [39, 40]. At this temperature, the photothermal effect acts in concert with the membrane-disrupting activities of released Ag^+ ions and PmB, eliciting a robust tripartite antimicrobial synergy that overcomes the formidable resistance of *P. aeruginosa*.

A benchmark comparison is summarized in Table S1 in the Electronic supplementary material (ESM). Most existing PDA- or Ag-based hydrogels fail to simultaneously address both drug-resistant infections and regenerative repair. Additionally, they are hindered by excessively high PTT temperatures and their inability to effectively resolve practical clinical challenges. Currently available products on the market are characterized by relatively weak and singular functionalities. The PmB/Ag-PDA@ECM hydrogel is anticipated to effectively eradicate PRPA infection *in vivo* while simultaneously accelerating the closure and healing of complex infected wounds, which provides an emerging clinical option for chronic wounds colonized by pathogenic bacteria.

2 Experimental

2.1 Synthesis and characterization of Ag-PDA nanoparticles

For the synthesis of PDA nanoparticles, 400 mg dopamine hydrochloride (Aladdin, D103111) was dissolved in 200 mL deionized water under stirring vigorously at 50 °C. Subsequently, 1.5 mL of 1 M NaOH solution was added. 5 h later, PDA nanoparticles were harvested using an ultrafiltration membrane (Millipore, 100 kDa) at 1000*g* for 25 min. The nanoparticles were then washed three times with pure water. Following lyophilization, the PDA nanoparticles were stored at 4 °C. For the synthesis of Ag-PDA nanoparticles, 300 mg $AgNO_3$ (Sinopharm Chemical Reagent, 10018464) was dissolved in 1.0 mL pure water. Ammonium hydroxide solution (Macklin, A801005) was added dropwise until the solution became clear at 0 °C. PDA nanoparticles were then added under dark conditions and the mixture was stirred for 1 h.

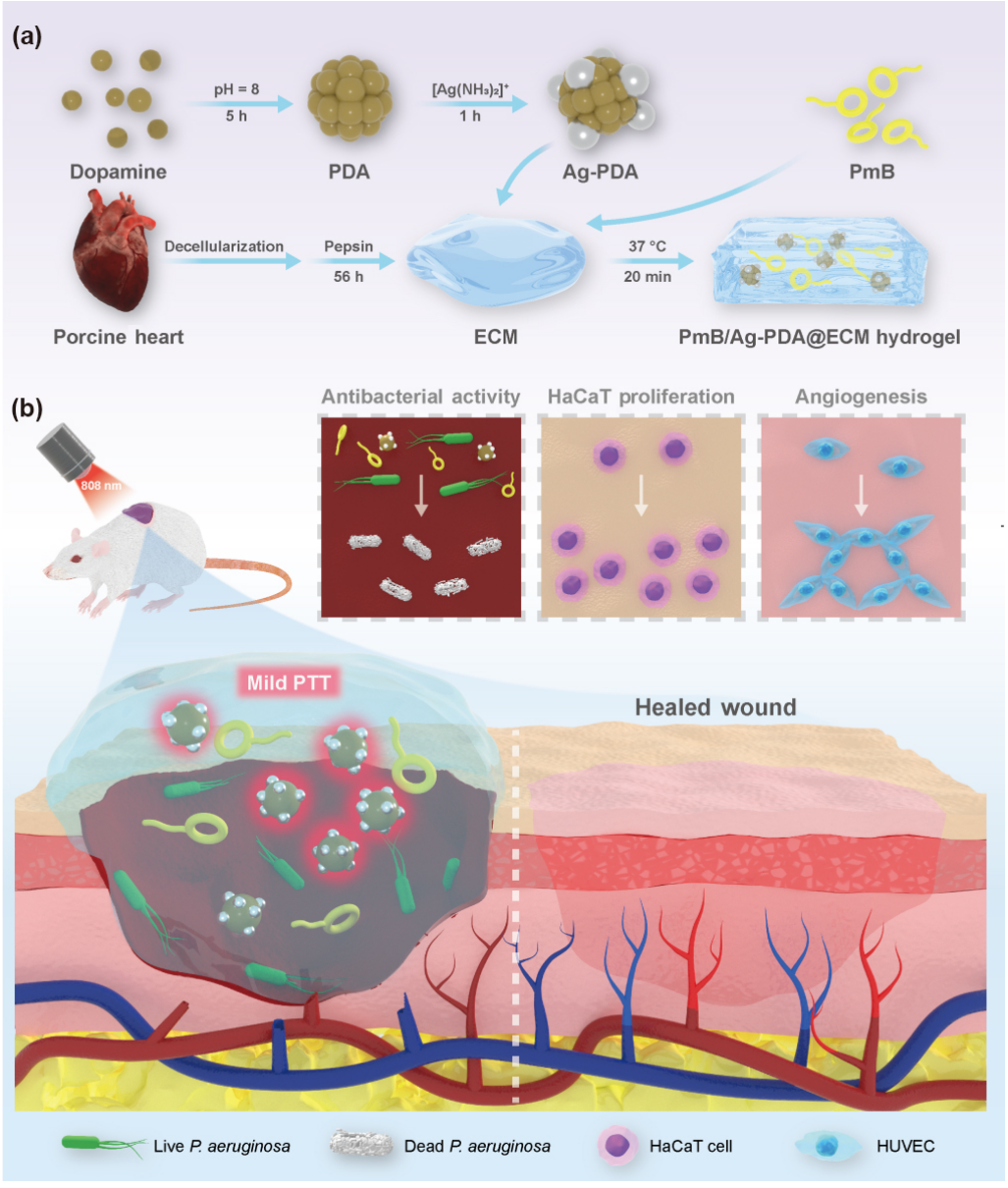

Scheme 1 Schematic illustration of the PmB/Ag-PDA@ECM hydrogel for PRPA-infected wound healing. (a) Dopamine undergoes spontaneous oxidative polymerization to form PDA NPs, which subsequently react with $[Ag(NH_3)_2]^+$ to yield Ag-PDA NPs. In parallel, a decellularized ECM derived from porcine myocardium is extracted and mixed with PmB. The resulting composite is formulated into the PmB/Ag-PDA@ECM hydrogel. (b) The synergistic antibacterial activity of PmB and Ag-PDA is enhanced by PTT, while the ECM component promotes the proliferation and migration of HaCaT cells and facilitates angiogenesis, collectively accelerating the healing of PRPA-infected wounds.

After the reaction, Ag-PDA nanoparticles were harvested using an ultrafiltration membrane (Millipore, 100 kDa) at 4000 rpm for 25 min. The nanoparticles were then washed three times with pure water. After lyophilization, the Ag-PDA nanoparticles were stored at 4 °C. Scanning electron microscopy (SEM, Zeiss G300, Germany) and transmission electron microscope (TEM) (JEOL JEM-1400flash, Japan) were used to investigate the morphologies of PDA and Ag-PDA nanoparticles. X-ray photoelectron spectroscopy (XPS) spectra and energy dispersive spectroscopy (EDS) were used to characterize the structure and composition of PDA and Ag-PDA nanoparticles.

2.2 Photothermal effect test

To systematically evaluate the photothermal properties, aqueous suspensions of the PDA NPs and Ag-PDA NPs were subjected to a series of characterizations. First, the concentration-dependent photothermal heating effect was assessed by irradiating suspensions at concentrations of 100, 200, 400, and 1000 μg·mL^{-1} with an 808 nm NIR laser (Lasever inc., China) at a power density of 1.0 W·cm^{-2} for 5 min. The temperature was recorded at 20 s intervals throughout the irradiation period. Next, the influence of laser intensity was investigated by exposing the nanoparticle suspensions (200 μg·mL^{-1}) to NIR irradiation at various power densities (0.5, 1.0, 1.5, and 2.0 W·cm^{-2}). Furthermore, the photothermal stability of the Ag-PDA NPs was examined over four consecutive heating/cooling cycles. For each cycle, the suspension was irradiated for 5 min before the laser was turned off, allowing the solution to cool naturally to ambient temperature. Throughout

the experiment, the beam diameter was maintained at 6 mm with a fixed sample-to-source distance of 2.5 cm.

2.3 Fabrication and characterization of extracellular matrix hydrogel

Porcine hearts were collected from local slaughterhouses, and the left ventricles were dissected and separated. After removing all fat and fascia, the left ventricles were cut up into small cubes with edge lengths of less than 2 mm. In order to decellularize the left ventricles, the tissue fragments were immersed in 1% wt·vol^{-1} sodium dodecyl sulfate (SDS) in phosphate buffered saline (PBS) and 1% Penicillin for a week. ECM was then washed with pure water until the decellularization solution was thoroughly removed. After decellularization procedure, ECM was lyophilized and ground into a powder. To assess the degree of decellularization, tissue samples before and after decellularization were stained with hematoxylin–eosin (H&E). With the aim of evaluating the collagen content, the samples were then stained with Masson's trichrome staining. For liquefying the ECM, pepsin (Sigma, P6887) was added to 0.1 M HCl solution and stirred for 30 min to ensure its dissolution. Then, ECM was added to the solution above and constantly stirred for 56 h at 25 °C. After 56 h, the liquid ECM was titrated with 5M NaOH to a pH of 7.4. Then, 10× PBS was applied to adjust the salt concentration to a final concentration of 1× PBS. The liquid was then frozen, lyophilized and stored at −80 °C. Then, the digested ECM was dissolved again in pure water and incubated at 37 °C for 20 min. After the gelation procedure, the ECM hydrogel formed.

2.4 Preparation and characterization of PmB/Ag-PDA@ECM

An appropriate amount of digested ECM, PmB, and Ag-PDA nanoparticles were added to pure water to achieve final concentrations of 20 mg·mL^{-1} for ECM, 1500 U·g^{-1} for PmB, and 200 μg·mL^{-1} for Ag-PDA. The mixture was magnetically stirred for 20 min and then incubated at 37 °C for 30 min to facilitate the formation of PmB/Ag-PDA@ECM. SEM (Zeiss G300, Germany) was utilized to examine the cross-sectional structure of the hydrogel, and the porosity was calculated using ImageJ software.

2.5 Swelling test

After lyophilization, the hydrogel was weighed (M_{dry}). Then it was immersed in deionized water preheated to 37 °C, and continued to swell at a constant temperature of 37 °C. At regular intervals, the hydrogel was removed, its moisture was wiped off, and its mass (M_{wet}) was measured. This process was repeated until the mass stabilized. The swelling rate of the hydrogel over time was plotted, and its equilibrium swelling rate was calculated (Eq. (1)).

$$\text{Swelling rate} = \frac{M_{wet}}{M_{dry}} \times 100\% \quad (1)$$

2.6 Erosion test

An appropriate amount of hydrogel was weighed and its mass was recorded. PBS solutions with pH values of 7.4 and 5.5 were added to separate samples of the hydrogel, which were then incubated at 37 °C under constant vibration. After 2 h of complete swelling, the hydrogel mass was measured again (M_0). The dissolution medium was continuously added, and at predetermined time intervals, the remaining mass of the hydrogel was recorded (M_T). This procedure was repeated, and the percentage of hydrogel dissolution was plotted against time to assess the dissolution behavior of the hydrogel in media with varying pH levels (Eq. (2)).

$$\text{Erosion rate} = \frac{M_T}{M_0} \times 100\% \quad (2)$$

2.7 *In vitro* degradation test

An appropriate amount of hydrogel was weighed and its mass was recorded (M_0). The enzyme degradation medium was prepared with collagenase type I solutions at concentrations of 5 and 10 U·mL^{-1}, and preheated to 37 °C. An adequate volume of each collagenase solution was added to fully immerse the hydrogel, which was then incubated at 37 °C under constant temperature. At predetermined time points, the liquid was removed, the remaining hydrogel mass was weighed (M_T). This process was repeated until the hydrogel was degraded completely. The degradation of the hydrogel in different collagenase media was assessed by plotting the percentage of hydrogel degradation over time (Eq. (3)).

$$\text{Degradation rate} = \frac{M_T}{M_0} \times 100\% \quad (3)$$

2.8 Mechanical performance tests

Rheological property evaluation: The hydrogel was molded into a cylindrical geometry (diameter: 1 cm, height: 2 mm). The storage modulus (G'), loss modulus (G''), and viscosity were measured using a rotational rheometer (Haake Mars 60, Thermo Fisher Scientific, Germany). Rheological characterization was performed at 37 °C, including a strain sweep (0.1%–1000%, 1 Hz) and a dynamic frequency sweep (0.1–100 Hz) at a constant strain of 1%.

Adhesive performance test: Two pieces of porcine skin, each measuring 1.5 × 0.5 cm^2, were overlapped with hydrogel applied at the interface. The ends of the skin were clamped in a universal material testing machine (NSS, C41.104) with a 100 N tension sensor at room temperature. The adhesive force generated by the hydrogel under tensile loading was evaluated (Eq. (4)).

$$\text{Stress (kPa)} = W_{max} \times S \quad (4)$$

2.9 Drug release analysis

The sample was enclosed in a dialysis bag (molecular weight cut-off: 3000 Da) and immersed in a PBS solution (pH 5.5) at a constant temperature of 37 °C. At predetermined time intervals (0.5, 1, 2, 3, 4, 6, 8, 12, 18, 24, and 48 h), 1000 μL of the PBS was collected and the dissolution medium was replenished with fresh PBS. The concentration of PmB was subsequently determined using UV spectrophotometry.

2.10 Ag^+ release analysis

To evaluate the sustained-release profile of silver ions, 1.0 g of the PmB/Ag-PDA@ECM hydrogel was sealed within a dialysis bag (molecular weight cut-off: 3000 Da) and subsequently submerged in 10 mL of phosphate-buffered saline (PBS, pH 5.5) to simulate an acidic microenvironment. As a comparative control, an equivalent concentration of Ag-PDA solution was similarly processed. The release media were maintained at a constant temperature of 37 °C under continuous agitation to maintain sink conditions. At

predetermined time intervals (1, 2, 4, 8, 12, 24, 48, and 72 h), 200 μL aliquots were withdrawn from the external buffer and replaced with an equal volume of fresh pre-warmed PBS. The concentration of Ag^+ in the collected samples was quantitatively determined using inductively coupled plasma mass spectrometry (ICP–MS). All experiments were performed in triplicate.

2.11 Cell proliferation test

Human immortalized keratinocytes (HaCaT) cells and human umbilical vein endothelial cells (HUVECs) were employed as model cells. Cells were seeded into 24-well plates at a density of 5×10^4 cells per well in 1.5 mL of complete culture medium. Subsequently, 200 μL of hydrogel samples were loaded into transwell inserts and irradiated with NIR light until the medium temperature reached 50 °C (the beam diameter was maintained at 6 mm with a fixed sample-to-source distance of 2.8 cm), followed by co-incubation with the cells at 37 °C. Cell viability was assessed at 24 and 48 h using the cell counting kit-8 (CCK-8) assay, following the manufacturer's instructions.

2.12 *In vitro* hemolysis test

Erythrocytes were isolated from defibrinated sheep blood (HopeBio, China) via centrifugation at 845*g* for 15 min and washed three times with Dulbecco's phosphate-buffered saline (D-PBS). Subsequently, 200 μL of Triton-X, D-PBS and extracts from different hydrogel (ECM, PmB@ECM, Ag-PDA@ECM, and PmB/Ag-PDA@ECM) were added to 0.8 mL of diluted erythrocytes. The mixtures were incubated at 37 °C for 4 h, followed by centrifugation at 845*g* for 10 min. The supernatants were collected, and their absorbance at 540 nm was measured to determine the hemolysis rate using the provided equation (Eq. (5)).:

$$\text{Hemolysis}\,(\%) = \frac{(OD_t - OD_n)}{(OD_p - OD_n)} \times 100\% \quad (5)$$

where OD_t is optical density (OD) value of tested samples, OD_n is OD value of negative control, and OD_p is OD value of positive control.

2.13 *In vitro* hemostasis test

The procoagulant activity of the hydrogels was assessed via a static whole blood clotting assay. Hydrogel samples were first prepared in the wells of a 24-well plate and pre-warmed to 37 °C. Fresh whole blood was collected from healthy BALB/c mice and anti-coagulated with sodium citrate. To begin the assay, a 50 μL aliquot of the citrated whole blood was gently applied to the surface of each pre-warmed hydrogel and incubated for 5 min at 37 °C. Clotting was then initiated by the addition of 10 μL of 0.2 M calcium chloride ($CaCl_2$) solution, followed by an additional 5 min incubation period. Subsequently, 5 mL water was added to each well and incubated for a final 5 min to lyse any non-clotted red blood cells. The resulting supernatant was carefully collected and subsequently centrifuged at 845*g* for 1 min to pellet the stable blood clots. The absorbance of the supernatant, which contains hemoglobin from the lysed, un-trapped red blood cells (RBCs), was measured at a wavelength of 540 nm. A lower absorbance value is indicative of less free hemoglobin and thus reflects a greater degree of clotting. The blood clotting index (BCI) was calculated using the following equation (Eq. (6)):

$$\text{BCI}\ (\%) = \frac{A_e}{A_n} \times 100\% \quad (6)$$

where A_e is the absorbance of the hemoglobin solution in the experimental group and A_n is the absorbance of the hemoglobin solution of the negative control group without other treatments.

2.14 *In vivo* hemostasis test

All animal protocols were approved by the Institutional Animal Care and Use Committee of Zhejiang University in this study. Male BALB/c mice (seven weeks old, 20–25 g) were randomly assigned to five treatment groups (n = 3 per group). Prior to the procedure, each mouse was anesthetized via isoflurane inhalation. To establish a tail hemorrhage model, approximately one-third of the distal tail was transected with sterile surgical scissors. The wound was allowed to bleed freely for approximately 10 s to confirm active hemorrhage. Subsequently, the amputated tail stump was gently covered with the respective hydrogel formulation. Blood loss was quantified by recording the change in mass of a pre-weighed piece of filter paper positioned beneath the tail. The time to hemostasis was also recorded, with the hemostatic endpoint defined as the complete cessation of bleeding from the hydrogel-wound interface for over 30 s.

2.15 *In vitro* antibacterial ability assay

The antibacterial properties of the hydrogel were assessed using the colony forming unit (CFU) assay and Live/Dead staining, with bacterial morphology examined via SEM.

Colony forming unit assay: *P. aeruginosa* P2550 in the logarithmic growth phase was harvested from Mueller-Hinton Agar (MHA) plates. The bacterial suspension was adjusted to 0.5 McFarland turbidity (approximately 1.5×10^8 CFU·mL^{-1}) using 0.9% saline and subsequently diluted to 5×10^5 CFU·mL^{-1}. A 200 μL aliquot of the hydrogel was added to a transwell insert (Biosharp, China) within a 24-well plate and incubated at 37 °C for gelation. Then, 1000 μL of the bacterial suspension was introduced per well, followed by irradiation with NIR (2.0 W·cm^{-2}, the beam diameter was maintained at 6 mm with a fixed sample-to-source distance of 2.5 cm) for 5 min. After 16 h of co-incubation, the suspension was diluted, plated onto MHA medium, and incubated at 37 °C for 24 h. Colonies were counted to calculate the bacterial viability.

Bacterial Live/Dead staining: Bacterial suspensions (5×10^5 CFU·mL^{-1}) were incubated at 37 °C for 12 h, followed by the addition of various hydrogels. The samples were then irradiated with NIR light and further incubated for 16 h. Subsequently, the bacterial cells were washed three times and resuspended in saline. A staining solution (G-Clone EX3000, China) was added to the suspension, which was incubated in the dark at room temperature for 15 min. The stained bacteria were then imaged using inverted laser scanning confocal microscope (Olympus FV1000, Japan).

Bacterial morphological characterization: Bacteria were incubated with various hydrogels for 16 h. The centrifuged bacteria were then fixed with 2.5% glutaraldehyde at 4 °C for 12 h. Following dehydration with a gradient of ethanol and drying, the morphology of the hydrogel-treated bacteria was observed using SEM (Zeiss G300, Germany).

Time-killing curves: Hydrogel samples were incubated with 4 mL of bacterial suspension at an initial concentration of 5×10^5 CFU·mL^{-1} at 37 °C. At predetermined time points (0, 2, 4, 6, 8, 12, 18, and 24 h), 100 μL aliquots of the suspension were collected and subjected to tenfold serial dilutions. From each

dilution, 10 μL was plated onto MHA plates. After incubation at 37 °C for 16–18 h, colonies were counted to determine the number of viable bacteria. The data were plotted to construct time-killing curves.

Biofilm inhibition assay: 800 μL of hydrogel was added to 4 mL of a bacterial suspension (5×10^5 CFU·mL^{-1}) in a test tube. The mixture was irradiated with near-infrared light (2.0 W·cm^{-2}) for 5 min and then incubated at 37 °C for 72 h. Planktonic bacteria were removed by washing with sterile water, and the tube was dried. Subsequently, 5 mL of 0.1% crystal violet solution was added and incubated at 37 °C for 15 min. After three washes with sterile water and drying, the crystal violet was dissolved in 30% acetic acid, and the biofilm mass was quantified by measuring absorbance at 595 nm.

2.16 Live cell staining test

HaCaT cells (2×10^4 cells per well) were seeded in 24-well plates and co-incubated with different hydrogels via transwell inserts. After near-infrared light irradiation (2.0 W·cm^{-2}) for 5 min, the cells were cultured for 24 h. The cells were then washed with PBS and stained with Calcein-AM (Beyotime C2015S, China). Fluorescence images were acquired using a fluorescence microscope (Olympus IX83, Japan).

2.17 Cell migration test

HaCaT cells (1 mL, 5×10^5 cells·mL^{-1}) were seeded into 24-well plates and incubated at 37 °C with 5% CO_2 until confluence. A scratch was made using a 200 μL pipette tip, and the wells were rinsed three times with PBS to remove detached cells. Cells were then co-incubated with different hydrogels for 24 h. Cell migration was recorded at 0 and 24 h using a fluorescence microscope (Olympus IX83, Japan). Migration rates were quantified using ImageJ software.

2.18 Tube formation test

A 1:1 mixture of plurigel matrix (Vazyme GL101, China) and RPMI 1640 medium (Meilun, China) was prepared, and 300 μL was evenly added to each well of a 24-well plate. After incubation at 37 °C for 1 h, HUVEC cells (5×10^5 cells per well) were seeded onto the matrix. Each hydrogel group was added to the transwell insert. Following 5 min of near-infrared irradiation, cells were then incubated at 37 °C for 5 h. HUVEC blood vessels formation was observed using a fluorescence microscope (Olympus IX83, Japan), and the total tube length and branching points were quantified using ImageJ.

2.19 *In vivo* healing of full-thickness PRPA-infected wounds tests

Healthy BALB/c mice (male, 6 weeks old, 20–25 g) were randomly divided into five groups: Control, ECM, PmB@ECM, Ag-PDA@ECM, and PmB/Ag-PDA@ECM. After depilation, a full-thickness circular wound with a diameter of 1 cm was excised on the dorsal side of each mouse. To establish the infected wound model, 100 μL of a *P. aeruginosa* P2550 suspension (1×10^7 CFU·mL^{-1}) was administered directly onto the wound.

Wound closure was monitored by photographing the wound site every other day. For bacterial load assessment, the wound area was swabbed five times with a saline-moistened cotton swab, which was then immersed in 1 mL of sterile saline. Following thorough vortexing and 10-fold serial dilutions, aliquots were plated on MHA and incubated for 16–18 h before colony counting.

A fresh hydrogel dressing was applied prior to each treatment, followed by NIR irradiation (2.0 W·cm^{-2}, 5 min, the beam diameter was maintained at 6 mm with a fixed sample-to-source distance of 2.5 cm). On day 3 post-injury, skin tissues were collected for immunofluorescence staining of pro-inflammatory markers TNF-α and IL-6. On day 14, histological assessments were performed on tissue sections from three mice per group. H&E staining was used to evaluate wound healing, while Masson's trichrome staining revealed collagen deposition. Immunofluorescence staining for Ki67 and CD31 was further conducted to assess cellular proliferation and neovascularization, respectively. For day 3, tissue samples were taken from around the wound margin, whereas on day 14, sections were taken along the wound diameter.

2.20 Statistical analysis

Statistics as well as graphical representations were performed using GraphPad Prism 10 software (GraphPad Software Inc., USA). All the results in this study were presented as the means ± standard deviations. At least three independent experiments were performed for all experiments, and representative images are shown. Comparisons between two groups were performed using Student's test. Comparisons between more than two groups were analyzed by a one-way ANOVA test. $P < 0.05$ was considered statistically significant.

3 Results and discussion

3.1 Synthesis and characterization of Ag-PDA and ECM hydrogel

To verify the successful incorporation of AgNPs onto PDA surfaces (Scheme 1(a)), the synthesized nanoparticles were examined via SEM and TEM (Figs. 1(a) and 1(b)). The SEM images demonstrate that, in contrast to the relatively smooth morphology of the PDA nanoparticles, the Ag-PDA nanoparticles exhibit a rougher surface with smaller nanoparticles attached. The statistical analysis of particle size distribution, as shown in Fig. S1 in the Electronic Supplementary Material (ESM), indicates a relatively uniform size distribution. TEM images further validate that the spherical PDA core structure of the Ag-PDA NPs consists of spherical PDA cores, with AgNPs, approximately 10–20 nm in size, uniformly distributed on the surface. EDS images provided supporting evidence of the presence of Ag in the Ag-PDA NPs (Fig. 1(c)). XPS spectra of the Ag-PDA NPs (Fig. 1(d)) display distinct signals corresponding to the C 1s (284 eV), N 1s (399 eV), and O 1s (532 eV) associated with PDA. Notably, two prominent peaks for Ag 3d at 367 and 373 eV were observed, corroborating the successful surface deposition of the presence of metallic silver on the PDA surface. The hydrodynamic diameters of PDA and Ag-PDA nanoparticles were determined via dynamic light scattering (DLS) to be 130.99 ± 9.89 and 185.18 ± 0.69 nm, respectively, consistent with the particle sizes observed in TEM images. The zeta potential of PDA NPs was measured at −19.93 ± 1.60 mV (Fig. 1(e)). Upon the integration of positively charged AgNPs, the zeta potential of Ag-PDA NPs increased to −13.27 ± 2.65 mV, indicating effective nanoparticle functionalization.

The photothermal conversion performance of the nanoparticles was systematically evaluated across a range of concentrations and NIR laser power intensities (Fig. 1(f) and Fig. S1 in the ESM). The analysis demonstrated a positive correlation between the

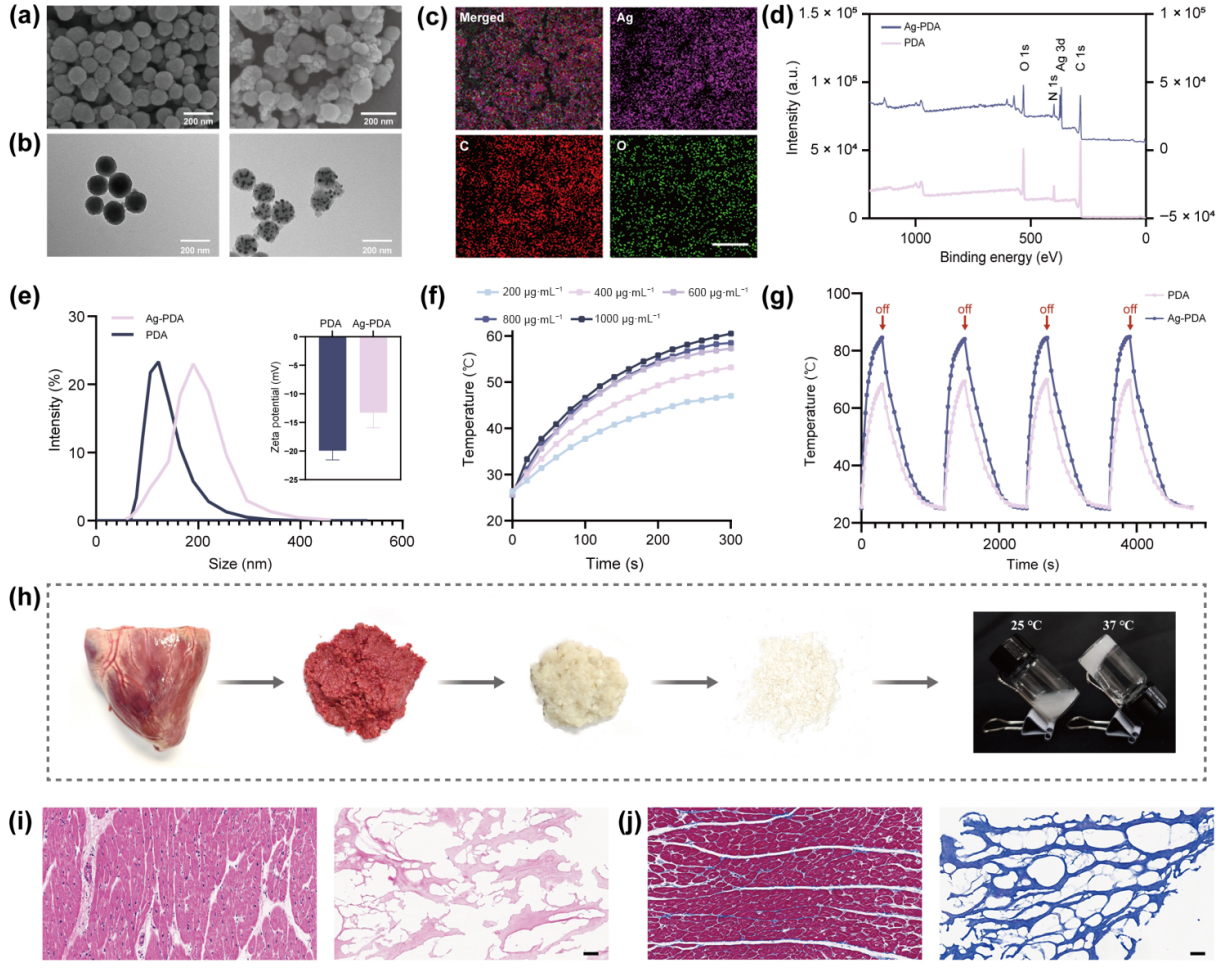

Figure 1 Synthesis and characterization of Ag-PDA and ECM hydrogel. (a) SEM images of PDA NPs (left) and Ag-PDA NPs (right). Scale bars: 200 nm. (b) TEM images of PDA NPs (left) and Ag-PDA NPs (right). Scale bars: 200 nm. (c) EDS elemental mapping of Ag-PDA NPs. Scale bars: 2.5 μm. (d) XPS spectra of PDA NPs and Ag-PDA NPs. (e) DLS analysis and zeta potential measurements of PDA NPs and Ag-PDA NPs (n = 3). (f) Photothermal performance of Ag-PDA NPs at varying concentrations under NIR laser irradiation. (g) Photothermal stability of PDA NPs and Ag-PDA NPs across four on/off NIR laser irradiation cycles. (h) Schematic representation of the preparation of a thermosensitive ECM hydrogel derived from porcine myocardium. (i) H&E staining and (j) Masson's trichrome staining of porcine cardiac tissue before and after decellularization. Scale bars: 50 μm.

photothermal response and both nanoparticle concentration and laser power. Figure 1(g) further demonstrates the reversible switching of the photothermal effect under on/off NIR irradiation, with consistent temperature elevation over four cycles, highlighting the excellent thermal stability and reusability of the Ag-PDA NPs.

We engineered a thermosensitive ECM hydrogel using a multi-step protocol including tissue mincing, decellularization, lyophilization, milling, and finally, pepsin digestion (Fig. 1(h)). The successful generation of an acellular scaffold is a critical prerequisite for its biomedical application. Indeed, histological evaluations using H&E and Masson's trichrome staining confirmed the complete decellularization from the ECM framework (Figs. 1(i) and 1(j)).

3.2 Characterization of PmB/Ag-PDA@ECM hydrogel

The optimal concentration of Ag-PDA NPs was determined to be 200 μg·mL^{-1} through an optimization of photothermal efficacy and biocompatibility, as evaluated by the CCK-8 assay (Fig. S2 in the ESM). The successfully prepared PmB/Ag-PDA@ECM hydrogel is shown in Fig. 2(a). The internal microstructure of the hydrogel was investigated using SEM. As shown in Fig. 2(b), the hydrogel exhibits a porous architecture with moderate porosity measured at 49.24% and an average pore size of 28.3 μm. Higher magnification images confirmed the uniform dispersion of Ag-PDA NPs within the hydrogel matrix.

The *in vitro* drug release profile was assessed in PBS at pH 5.5 to simulate the infected wound microenvironment. The PmB/Ag-PDA@ECM hydrogel displayed a rapid release of approximately 80% of the loaded PmB within 6 h, ensuring rapid therapeutic availability at the application site at the application site (Fig. 2(c)). Complementing this initial rapid effect, the release of silver ions exhibited a distinct sustained profile. As depicted in Fig. S2 in the ESM, the PmB/Ag-PDA@ECM hydrogel effectively circumvents the burst release of Ag^+ via physical barriers and electrostatic anchoring, sustaining a low yet steady concentration profile. This release behavior is pivotal for balancing prolonged bacteriostasis with minimal cytotoxicity toward host tissues. When coupled with the synergistic action of PmB, the system establishes a safe and persistent therapeutic microenvironment for the management of infected wounds. To further optimize sustained therapeutic levels for chronic wound management, future work will explore strategies to attenuate burst release and prolong PmB retention, such as tuning ECM concentration, introducing chemical cross-linking, or

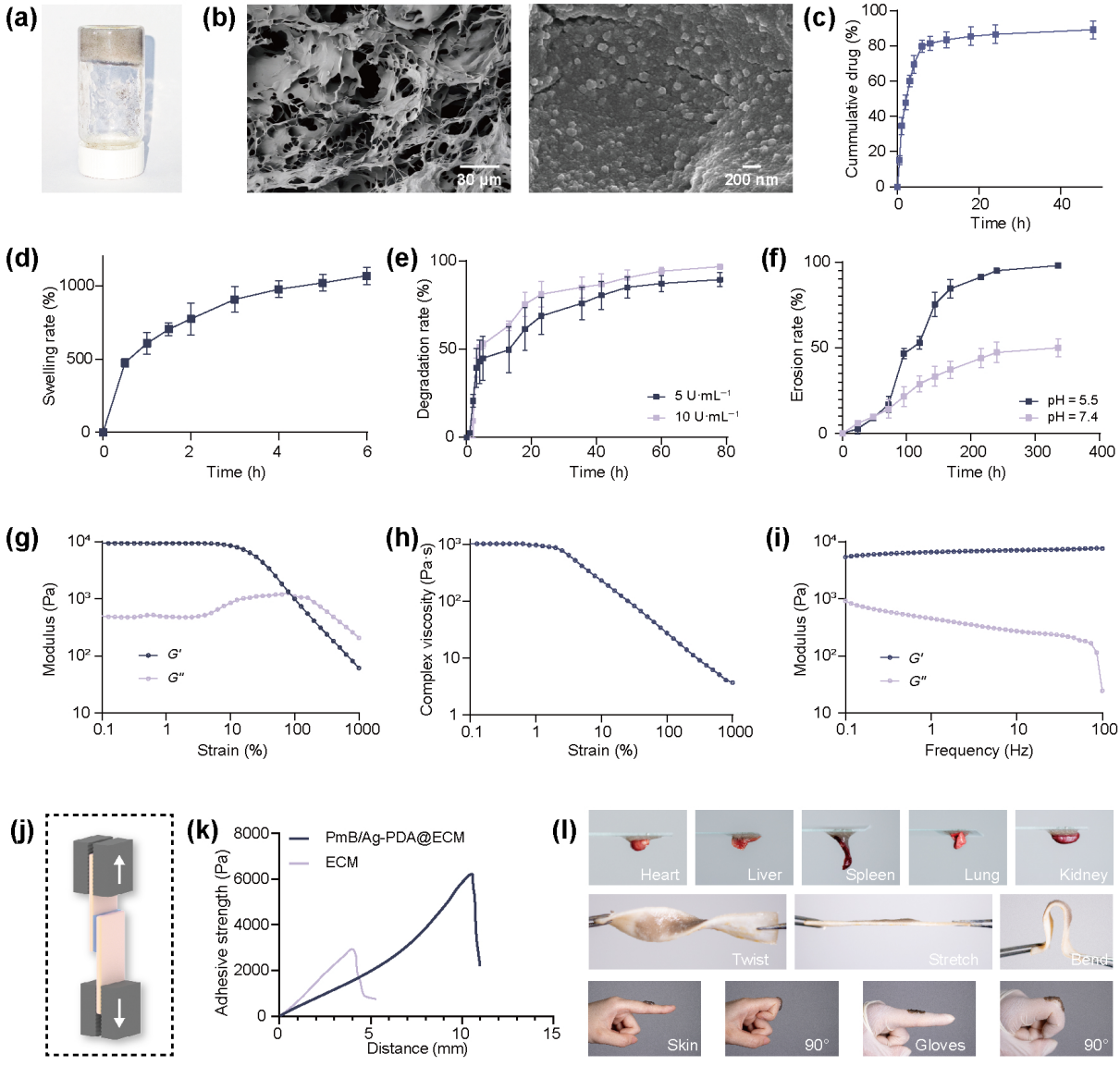

Figure 2 Characterization of PmB/Ag-PDA@ECM hydrogel. (a) Photograph of the PmB/Ag-PDA@ECM hydrogel. (b) SEM images of the PmB/Ag-PDA@ECM hydrogel. Scale bars: 30 μm (left), 200 nm (right). (c) The release profile of PmB from the PmB/Ag-PDA@ECM hydrogel. (d) Swelling rate, (e) degradation rate, and (f) erosion rate of the hydrogel (n = 3). (g) Rheology analysis of the PmB/Ag-PDA@ECM hydrogel in strain sweep experiment. (h) The viscosity curves of the PmB/Ag-PDA@ECM hydrogel. (i) Rheology analysis of the PmB/Ag-PDA@ECM hydrogel in dynamic frequency sweep experiment. (j) The scheme and (k) stress-strain profiles of ECM hydrogel and PmB/Ag-PDA@ECM hydrogel by tensile test. (l) Adhesion of the hydrogel on different surfaces.

strengthening drug-matrix interactions. The swelling test results indicated that the hydrogel exhibited rapid swelling capacity, reaching a swelling ratio of nearly 1068.21% ± 59.24% within 4 h (Fig. 2(d)). This excellent swelling and water-retention capacity allows for the efficient absorption of wound exudate, thereby maintaining a moist environment conducive to cell proliferation and tissue regeneration. Biodegradability is crucial for wound dressing applications, allowing the material to be replaced by new tissue during healing. As depicted in Fig. 2(e), the hydrogel underwent rapid degradation in the presence of collagenase (10 U·mL^{-1}), achieving a degradation rate of 96.98% ± 0.48% after 78 h. In contrast, the hydrogel demonstrated stability in the absence of enzymes, showing erosion levels of 97.93% ± 0.77% at pH 5.5 and 50.03% ± 5.35% at pH 7.4 after 14 days of incubation (Fig. 2(f)).

The rheological properties of the PmB/Ag-PDA@ECM hydrogel were first investigated by strain amplitude sweep tests. Within a wide strain range of 0.1% to 79.6%, both the storage modulus (G') and the loss modulus (G'') remained stable, with G' consistently higher than G'' (Fig. 2(g)). This behavior indicates that the hydrogel resides within its linear viscoelastic region (LVR), demonstrating notable structural integrity. Notably, the complex viscosity (η) of the hydrogel also remained stable across the same strain range, further corroborating its structural robustness (Fig. 2(h)). To further probe the viscoelastic nature, frequency sweep measurements were performed. The results revealed that G' was substantially greater than G'' over the entire frequency range of 0.1–100 Hz, indicative of a solid-like, predominantly elastic response. This characteristic response confirms the formation of a stable and well-defined three-dimensional network structure within the hydrogel (Fig. 2(i)). The incorporation of Ag-PDA was found to enhance the adhesive properties of the hydrogel. Lap-shear tests on

porcine skin tissue (Fig. 2(j)) revealed that the PmB/Ag-PDA@ECM hydrogel demonstrated enhanced adhesive strength (6.238 ± 0.13 kPa) compared to the pristine ECM hydrogel (2.953 ± 0.19 kPa) (Fig. 2(k)). This indicates that the PmB/Ag-PDA@ECM hydrogel can adhere firmly to the wound surface, facilitating its application and retention. The PmB/Ag-PDA@ECM hydrogel exhibited robust adhesion to a broad spectrum of substrates, including human skin, latex gloves, visceral tissues and porcine skin, and retained strong interfacial adhesion under mechanical stress (e.g., bending and twisting) without the need for external fixation (Fig. 2(l)). The strong adhesive capability of the hydrogel further enhances its potential for dynamic wound management and hemostasis.

3.3 Cytocompatibility, hemocompatibility and hemostatic efficacy

The cytocompatibility of PmB/Ag-PDA@ECM with HaCaT and HUVECs was first assessed via CCK-8 assays. As showed in Figs. 3(a) and 3(b), all hydrogel formulations, including ECM, PmB@ECM, Ag-PDA@ECM, and PmB/Ag-PDA@ECM, demonstrated improved viability compared to the Control group, indicating favorable compatibility of both the composite matrix and photothermal responsiveness of Ag-PDA. After 48 h of co-incubation, the PmB/Ag-PDA@ECM group exhibited cell viabilities of 124.14% ± 12.7% for HaCaT and 115.64% ± 1.53% for HUVECs, highlighting its capacity in promoting cell proliferation. Phalloidin staining of HaCaT cells revealed that all hydrogel groups maintained normal cytoskeletal architecture, further confirming excellent cytocompatibility (Fig. 3(c)). Hemocompatibility, evaluated via a hemolysis assay, demonstrated that all hydrogel groups showed hemolysis rates under 2%, confirming the blood compatibility of PmB/Ag-PDA@ECM (Fig. 3(d)). To evaluate the hemostatic performance of the hydrogel as a wound dressing, both *in vitro* and *in vivo* coagulation assays were conducted. To assess

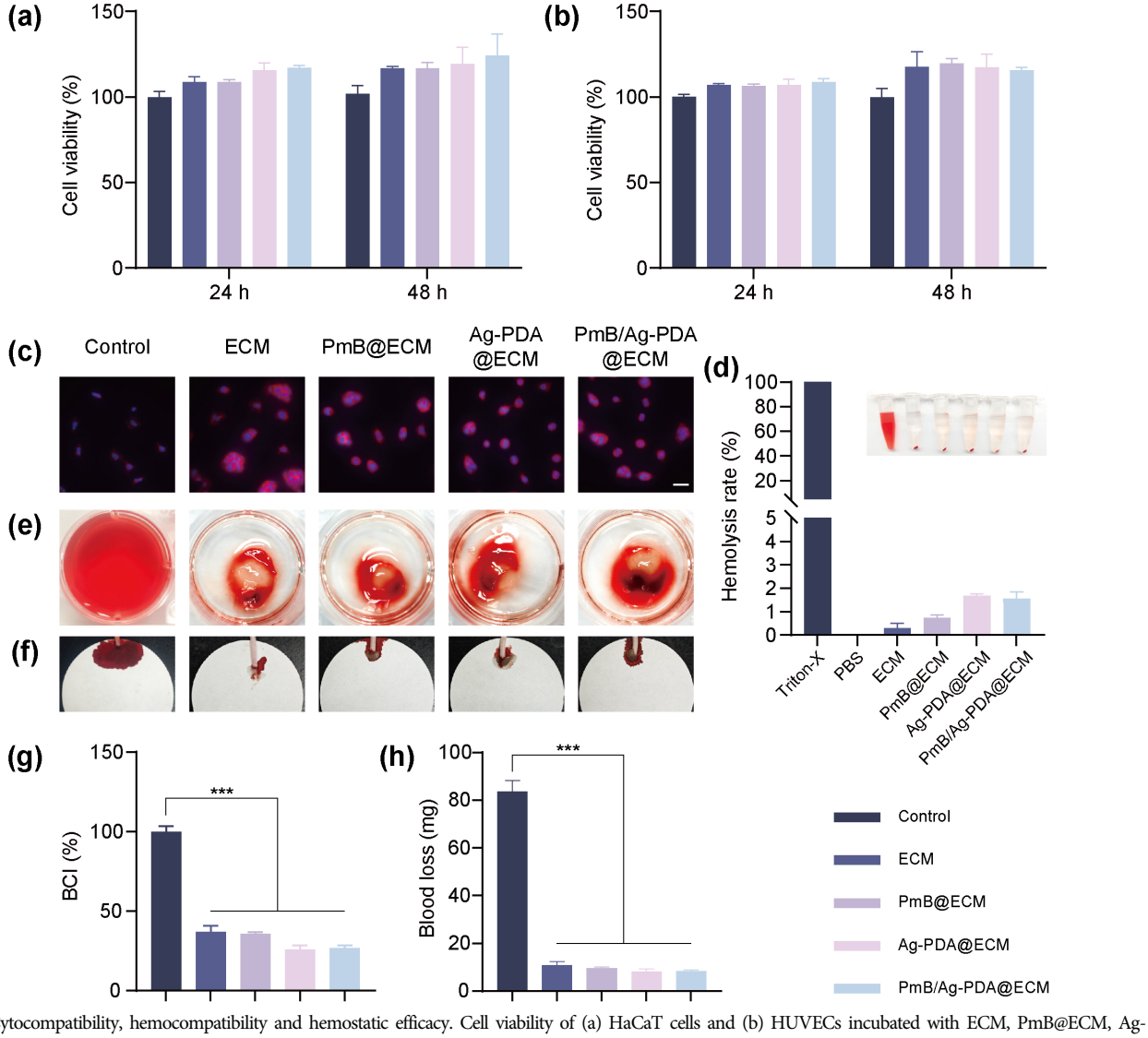

Figure 3 Cytocompatibility, hemocompatibility and hemostatic efficacy. Cell viability of (a) HaCaT cells and (b) HUVECs incubated with ECM, PmB@ECM, Ag-PDA@ECM, PmB/Ag-PDA@ECM (n = 3). (c) Cytoskeleton staining after 24 h incubation with different hydrogels. (d) Blood compatibility assessed via hemolysis assay (n = 3). Representative image inset (left to right): Triton-X, PBS, ECM, PmB@ECM, Ag-PDA@ECM, and PmB/Ag-PDA@ECM. (e) Photograph of *in vitro* hemostasis test. (f) Photograph of *in vivo* hemostasis test on mouse tail hemorrhage model. (g) BCI of different hydrogels (n = 3). (h) Quantitation of blood loss (n = 3). Statistical differences among groups were analyzed using one-way ANOVA followed by Tukey's post hoc test. Significance levels were defined as $^{*}P < 0.05$, $^{**}P < 0.01$, and $^{***}P < 0.001$ relative to the indicated group.

hemostatic efficacy, the blood clotting index (BCI) was measured (Figs. 3(e) and 3(g)). Both Ag-PDA@ECM and PmB/Ag-PDA@ECM exhibited substantially reduced BCI values, 25.77 ± 2.83 and 26.86 ± 1.60 respectively, indicating their superior clot-promoting ability. Consistently, using a murine tail bleeding model, these hydrogels effectively reduced bleeding, reinforcing the *in vitro* results (Figs. 3(f) and 3(h)). In summary, PmB/Ag-PDA@ECM exhibits excellent biocompatibility and hemostatic performance, highlighting its promise as a multifunctional wound dressing.

3.4 *In vitro* antibacterial activity

The minimum inhibitory concentration (MIC) and minimum bactericidal concentration (MBC) of PmB were initially evaluated against two strains of *P. aeruginosa*. For the drug-sensitive strain PSPA (*P. aeruginosa* ATCC 27853), the MIC and MBC were determined as 1 and 2 μg·mL^{-1}, respectively. In contrast, the resistant strain PRPA (*P. aeruginosa* P2550) exhibited considerably higher resistance, with MIC and MBC values of 8 and 16 μg·mL^{-1}, respectively. To evaluate the antibacterial efficacy of the hydrogels, both PSPA and PRPA strains were co-incubated with different hydrogels, followed by plate counting to quantify bacterial viability (Figs. 4(a) and 4(d)). Upon NIR irradiation, both Ag-PDA@ECM and PmB/Ag-PDA@ECM groups exhibited a marked reduction in bacterial survival compared to their non-irradiated counterparts, whereas the hydrogels lacking Ag-PDA showed negligible changes, indicating that NIR irradiation alone exerts minimal antibacterial effect. Notably, for the PRPA strain (P2550), which was not effectively inhibited by PmB@ECM or Ag-PDA@ECM individually, PmB/Ag-PDA@ECM hydrogel under NIR irradiation achieved full bacterial clearance, suggesting a potent synergistic antibacterial effect among PTT, PmB, and Ag-PDA. Live/Dead staining validated the superior antibacterial activity of PmB/Ag-PDA@ECM against PRPA (Fig. 4(b)). Post-incubation, live bacteria emitted green fluorescence, while dead bacteria showed red fluorescence; the PmB/Ag-PDA@ECM group displayed scant green signals and an increased red-to-green ratio than controls. SEM imaging (Fig. 4(c)) revealed intact bacterial morphology in control and ECM groups, whereas PmB@ECM and Ag-PDA@ECM induced mild membrane disruption. Furthermore, the PmB/Ag-PDA@ECM group exhibited substantial membrane destruction. The potent eradication of PRPA can be attributed to the synergistic mechanism that overcomes the intrinsic resistance of *P. aeruginosa*.

Time-dependent bactericidal efficacy was assessed via time-kill curves (Fig. 4(e)), which showed bacterial growth in control and ECM groups, with PmB@ECM and Ag-PDA@ECM only marginally reducing proliferation. In contrast, PmB/Ag-PDA@ECM demonstrated a ≥ 3log$_{10}$(CFU·mL^{-1}) reduction within 6 h and total elimination by 24 h. Crystal violet staining-based

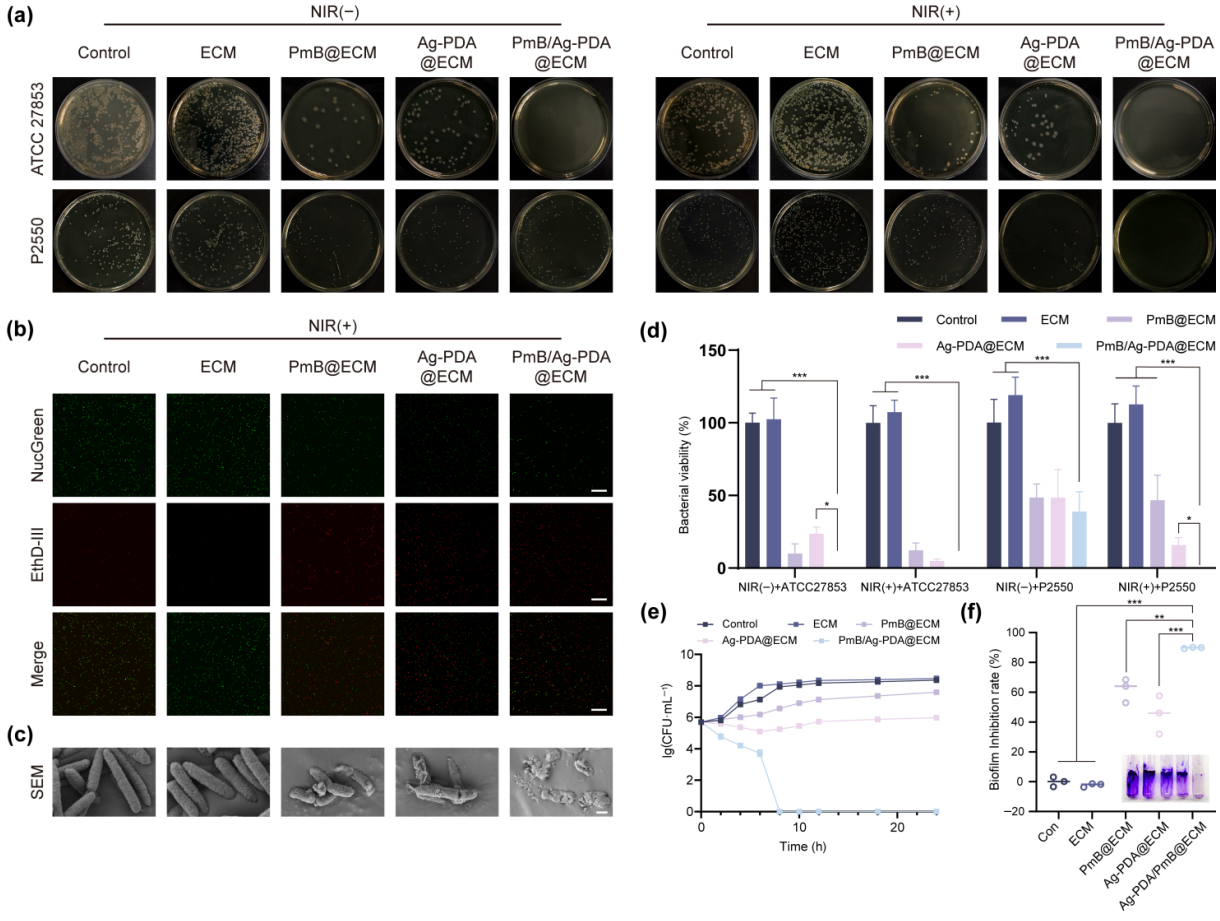

Figure 4 *In vitro* antibacterial activity. (a) Optical images of *P. aeruginosa* P2550 and ATCC27853 bacterial colonies after different treatments with/without NIR irradiation (2.0 W·cm^{-2}, 5 min). (b) Fluorescence images of the live/dead (green/red) bacteria treatment via different hydrogels with NIR irradiation (2.0 W·cm^{-2}, 5 min). (c) SEM images of *P. aeruginosa* P2550 after incubation with different hydrogels (n = 3). (d) Bacterial viability of *P. aeruginosa* after different treatments. (e) Time-kill curve of different hydrogels (n = 3). (f) Biofilm inhibition rate of different hydrogels (n = 3). Statistical differences among groups were analyzed using one-way ANOVA followed by Tukey's post hoc test. Significance levels were defined as *P < 0.05, **P < 0.01, and ***P < 0.001 relative to the indicated group.

biofilm assays (Fig. 4(f)) further demonstrated that the PmB/Ag-PDA@ECM hydrogel substantially inhibited *P. aeruginosa* P2550 biofilm formation, achieving an inhibition rate of 89.82% ± 0.43%, underscoring its robust bactericidal and anti-biofilm properties.

Typically, PRPA resistance arises from the modification of lipid A in the outer membrane, which reduces the negative charge and consequently the electrostatic affinity for cationic polymyxin B [41]. However, the mPTT (~ 50 °C) induced by the hydrogel increases the fluidity of the bacterial phospholipid bilayer and disrupts the function of efflux pumps, physically compromising the outer membrane barrier [42]. This thermal disruption acts as a permeabilization gate, allowing the sustained release of Ag^+ ions and PmB to bypass the membrane blockade and penetrate the cytoplasm efficiently [21]. Once intracellular, Ag^+ ions bind avidly to thiol groups (-SH) in metabolic enzymes and trigger the generation of reactive oxygen species (ROS), leading to irreversible DNA damage and respiratory chain collapse [43]. Therefore, the combined effects of thermal membrane destabilization, PmB and Ag^+-induced oxidative damage, collectively overwhelms the bacterial defense systems, preventing the development of resistance [44].

3.5 *In vitro* wound healing activity

As indicated by the CCK-8 assay, PmB/Ag-PDA@ECM markedly promoted cellular proliferation, which was further confirmed using a Live/Dead Kit. As shown in Fig. 5(a), compared to the Control group, all hydrogels induced pronounced green fluorescence, indicative of live cells, after 24 h of incubation. A scratch assay demonstrated that all hydrogel-treated groups exhibited enhanced cellular migration rates compared to the Control group (Figs. 5(b) and 5(d)). Additionally, angiogenesis assays revealed that all hydrogel groups remarkably promoted HUVEC formation of capillary-like structures, as evidenced by increased branch numbers and total length (Figs. 5(c), 5(e), and 5(f)). Notably, although all ECM-containing hydrogel formulations exhibited excellent pro-healing activity, no statistically significant differences in efficacy were observed among them. This suggests that in this bacteria-free *in vitro* cell model, the observed cell proliferation, migration, and angiogenesis are primarily attributable to the biological activity of the ECM matrix, while PmB, Ag-PDA, or the photothermal effect did not provide an additional, direct promoting effect in these specific aspects.

3.6 *In vivo* full-thickness PRPA-infected skin wound healing

A full-thickness skin wound model infected with PRPA was constructed on the backs of BALB/c mice and treated with the PmB/Ag-PDA@ECM hydrogel (Fig. 6(a)). The photothermal effect of the hydrogel within the wound was monitored using an infrared thermal imager during treatment (Fig. 6(b)). Following NIR irradiation (2.0 $W \cdot cm^{-2}$, 5 min), the Ag-PDA group hydrogel reached 49.7 °C, the PmB/Ag-PDA@ECM group reached 51.2 °C, whereas the hydrogel lacking Ag-PDA only warmed to the mouse body temperature (approximately 37 °C).

Wound photographs indicated that, on day 2, all groups except the PmB/Ag-PDA@ECM group exhibited remarkable yellow-green pus accumulation (Fig. 6(c)). To assess the hydrogels' antibacterial efficacy during infected wound healing, bacterial samples were collected from the wounds every two days, inoculated onto MHA plates, and quantified post-incubation. Results demonstrated that the PmB/Ag-PDA@ECM group exhibited significantly fewer bacterial colonies post-treatment compared to other groups, with no viable bacteria detected by day 6 (Fig. 6(g)). Conversely, the remaining four groups displayed varying degrees of bacterial proliferation, with viable bacteria nearly undetectable only after complete scabbing by day 10. These findings highlight the robust antibacterial performance of PmB/Ag-PDA@ECM.

Throughout the 14-day treatment, the PmB/Ag-PDA@ECM group exhibited the most rapid healing, reducing the wound area to 0.83 ± 0.53 mm^2 by day 14, nearly fully healed, while the other groups recorded areas of 42.02 ± 3.38, 25.42 ± 4.25, 12.27 ± 3.79, and 12.43 ± 4.36 mm^2, respectively (Figs. 6(d) and 6(h)). This highlights the superior capacity to accelerate wound healing of PmB/Ag-PDA@ECM.

Histopathological analysis of regenerated skin after 14 days of treatment was performed using H&E, Masson, CD31, and Ki67 immunohistochemical staining. Only the PmB/Ag-PDA@ECM group restored a complete epithelial structure, as illustrated in Fig. 6(e). Wound width measurements corroborated the wound area data (Fig. 6(i)). Collagen deposition, evaluated via Masson's staining, revealed abundant and well-organized collagen in the PmB/Ag-PDA@ECM group (Fig. 6(f)), with quantitative analysis of blue-stained regions indicating considerably higher collagen content compared to other groups (Fig. 6(j)). Neovascularization was assessed through CD31 immunohistochemistry, a marker of vascular endothelial cells (Fig. 7(a)), showing the highest blood vessel density in the PmB/Ag-PDA@ECM group, indicative of enhanced angiogenesis (Fig. 7(g)). Cell proliferation, evaluated via Ki67 staining (Fig. 7(b)), revealed the highest proportion of Ki67-positive cells in the PmB/Ag-PDA@ECM group, confirming its potent proliferative effect (Fig. 7(h)). Regeneration of skin appendages (hair follicles and sebaceous glands) was further assessed by keratin (KRT) 14 and KRT6 immunofluorescence, with complete appendage formation observed solely in the PmB/Ag-PDA@ECM group by day 14 (Fig. 7(c)).

By observing epidermal thickness in the H&E-stained sections on day 3, a preliminary assessment of the wound inflammation level could be made (Fig. 7(d)). To further evaluate anti-inflammatory properties, wound samples from day 3 underwent immunofluorescence staining for key inflammatory cytokines (IL-6 and TNF-α) and macrophage markers. The PmB/Ag-PDA@ECM group displayed marked downregulation of TNF-α and IL-6, indicating substantial suppression of the inflammatory microenvironment (Figs. 7(e), 7(i) and 7(j)). Staining for CD86 (M1 marker), CD206 (M2 marker), and CD68 (M0 marker) indicated that PmB/Ag-PDA@ECM promoted macrophage M2 polarization, with a reduced M1 ratio (0.65 ± 0.18), elevated M2 ratio (6.63 ± 0.49), and the lowest M1/M2 ratio (0.099 ± 0.032) (Figs. 7(f), and 7(k)–7(m)). Histological analysis via H&E staining of major organs, including the heart, liver, spleen, lungs, and kidneys, revealed no discernible histopathological abnormalities in any treatment group, further corroborating the high biocompatibility of the PmB/Ag-PDA@ECM hydrogel (Fig. S3 in the ESM).

4 Conclusions

In summary, we have successfully engineered a multifunctional hydrogel, designated as PmB/Ag-PDA@ECM, for the effective management of drug-resistant bacterial infections and the simultaneous promotion of wound regeneration. This hydrogel

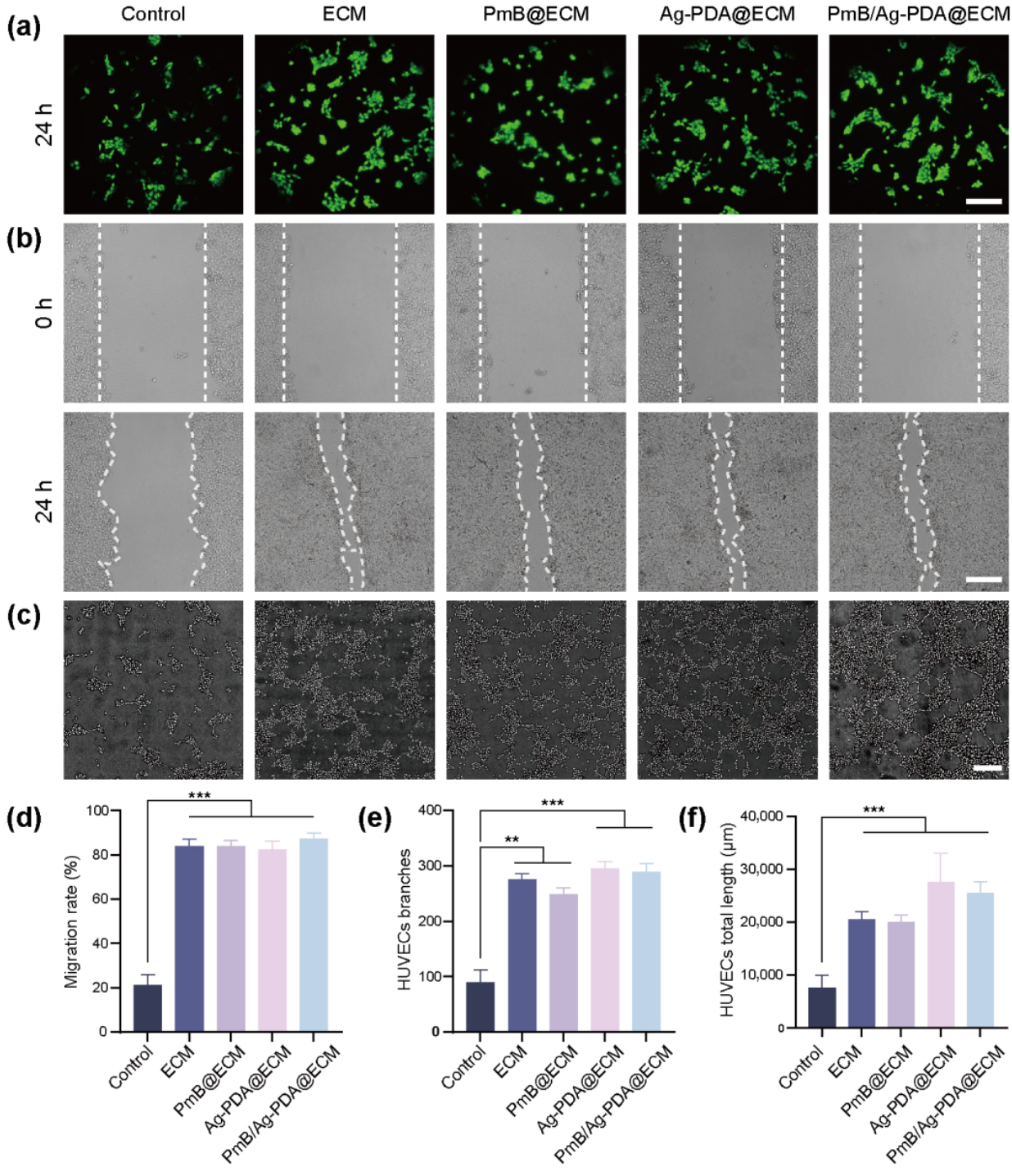

Figure 5 *In vitro* wound healing activity. (a) Live staining of HaCaT cells after different treatments. Green fluorescence represents living cells. Scale bars: 200 μm. (b) Images of HaCaT cells migration at 0 and 24 h. Scale bars: 200 μm. (c) Images of HUVECs angiogenesis. Scale bars: 200 μm. (d) HaCaT cells' migration rate with different treatments (n = 3). (e) Quantitative analysis of HUVECs branches (n = 3). (f) Quantitative analysis of HUVECs total length (n = 3). Statistical differences among groups were analyzed using one-way ANOVA followed by Tukey's post hoc test. Significance levels were defined as $^{*}P < 0.05$, $^{**}P < 0.01$, and $^{***}P < 0.001$ relative to the indicated group.

showcases a suite of advantageous properties, including remarkable photothermal conversion efficiency, thermosensitivity, a highly porous internal architecture, biodegradability, and excellent biocompatibility. *In vitro*, the NIR-triggered photothermal effect, coupled with the synergistic action of PmB and Ag-PDA, enabled the PmB/Ag-PDA@ECM hydrogel to achieve complete eradication of PRPA. The PmB/Ag-PDA@ECM hydrogel enhanced the proliferation and migration of HaCaT cells, and promoted the angiogenesis of HUVECs *in vitro*. *In vivo* studies corroborated these findings, confirming the dual efficacy of the hydrogel in combating drug-resistant infections and accelerating wound healing. Collectively, this work presents a promising candidate for the clinical management of infected wounds and offers a versatile platform for advanced therapeutic applications.

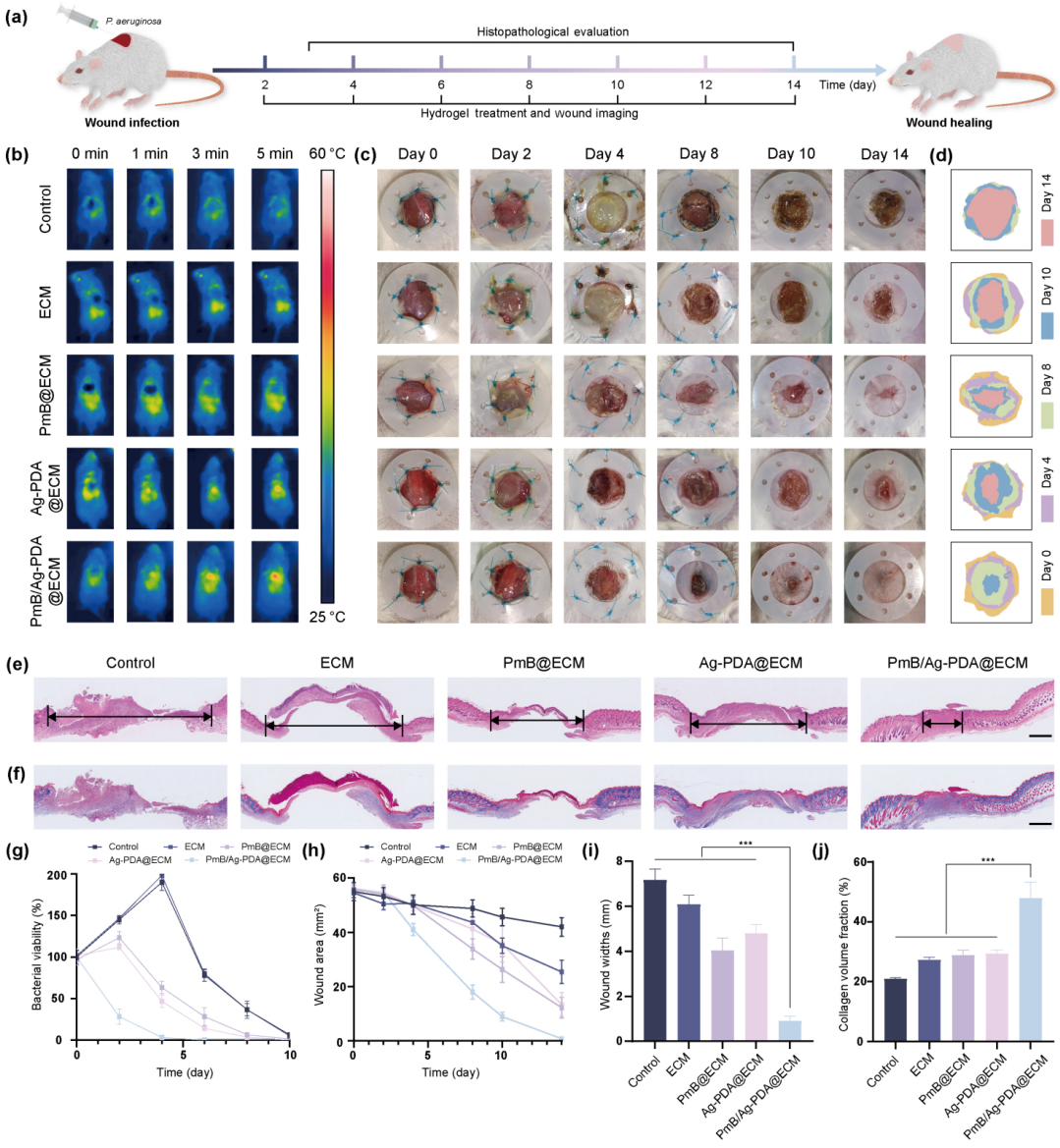

Figure 6 Acceleration of PRPA-infected wound healing by PmB/Ag-PDA@ECM. (a) Schematic diagram of infected wound creation, treatment and skin wound harvest timeline in BALB/c mice. (b) Infrared thermal images on mice. (c) Representative images of the wound area by different treatments on days 0, 2, 4, 8, 10 and 14 after operation. (d) Schematic images of wound contraction with different treatments from days 0 to 14. (e) Representative images of H&E staining of wound sections after 14 days of treatment. Scale bar: 500 μm. (f) Representative images of Masson staining of wound sections after 14 days of treatment. Scale bar: 500 μm. (g) Bacterial viability curve from day 0 to 14 (n = 3). (h) Quantification of wound area from days 0 to 14 (n = 3). (i) Quantification of wound widths in H&E staining (n = 3). (j) Quantification of collagen deposition in Masson staining (n = 3). Statistical differences among groups were analyzed using one-way ANOVA followed by Tukey's post hoc test. Significance levels were defined as $^{*}P < 0.05$, $^{**}P < 0.01$, and $^{***}P < 0.001$ relative to the indicated group.

Electronic Supplementary Material: Supplementary material (comparison of representative hydrogel systems and the present work, photothermal performance of Ag-PDA and PDA, cell viability after incubation with different concentrations of Ag-PDA and histopathological images of viscera) is available in the online version of this article at https://doi.org/10.26599/NR.2026.94908546.

Data availability

All data needed to support the conclusions in the paper are presented in the manuscript and/or the Electronic Supplementary Material. Additional data related to this paper may be requested from the corresponding author upon request.

Acknowledgements

None.

Declaration of competing interest

All the contributing authors report no conflict of interests in this work.

Author contribution statement

J. L. L.: Investigation, methodology, data analysis, writing original draft. C. L. S.: Methodology, conceptualization. Y. Z. J.: Data curation. Q. Z.: Methodology, data analysis. J. W. Z.: Investigation,

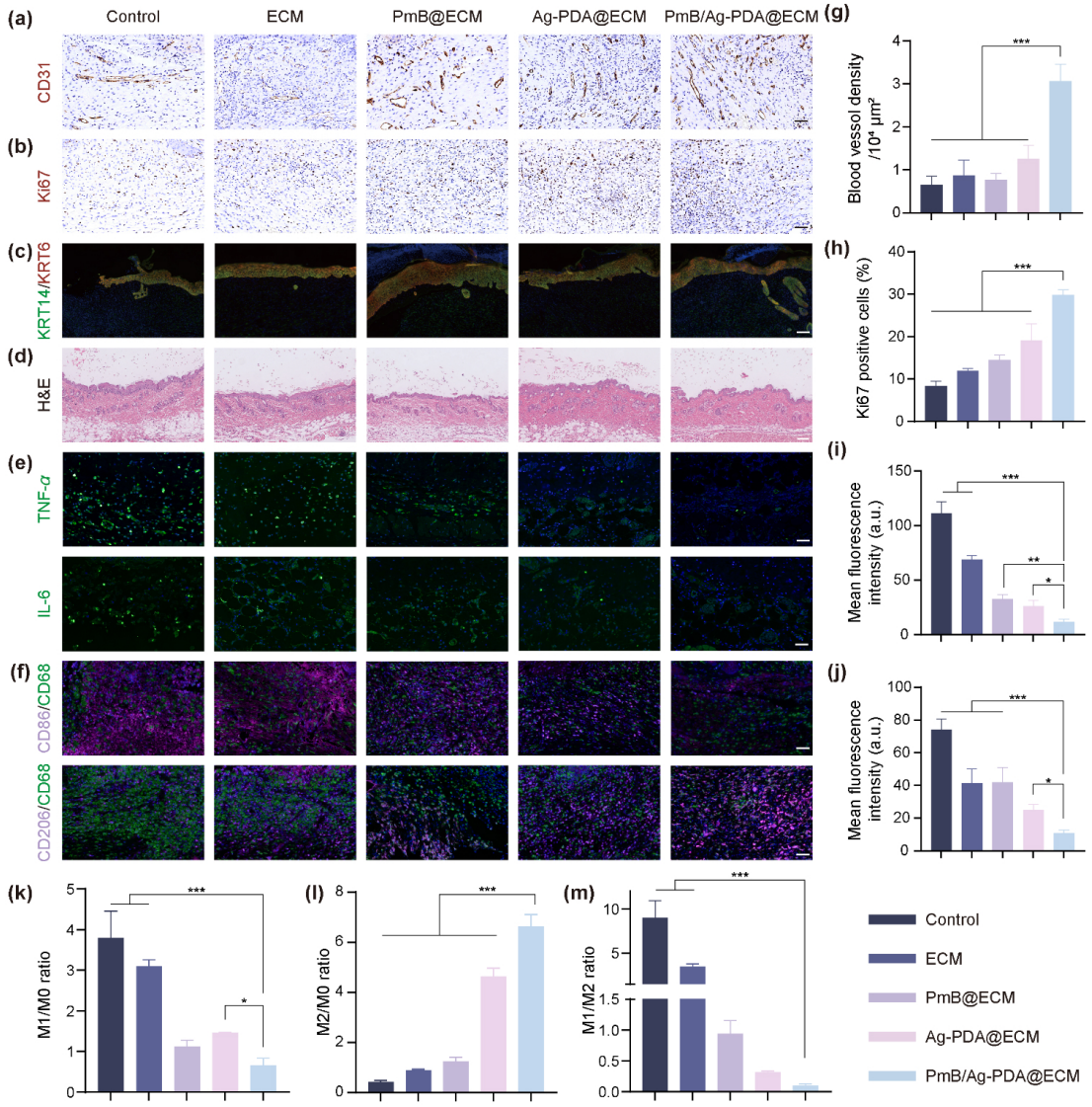

Figure 7 Evaluation of PRPA-infected wound healing. (a) Images of immunohistochemical staining of CD31. Scale bar: 200 μm. (b) Images of immunohistochemical staining of Ki67. Scale bar: 200 μm. (c) Immunofluorescence staining of KRT6 (hyperplastic epidermis) and KRT14 (normal epidermis). Scale bar: 100 μm. (d) Representative images of H&E staining of wound sections after 3 days of treatment. Scale bar: 100 μm. (e) Immunofluorescence staining of TNF-α and IL-6. Scale bar: 200 μm. (f) Immunofluorescence staining of CD86 (M1 marker), CD206 (M2 marker), and CD68 (M0 marker) on day 3. Scale bar: 200 μm. Quantitative analyses of (g) CD31, (h) Ki67, (i) TNF-α, and (j) IL-6 Immunofluorescence staining ($n = 3$). Quantification of immunofluorescence staining of the (k) M1/M0 ratio, (l) M2/M0 ratio, and (m) M1/M2 ratio of different treatments on day 3 ($n = 3$). Statistical differences among groups were analyzed using one-way ANOVA followed by Tukey's post hoc test. Significance levels were defined as $^{*}P < 0.05$, $^{**}P < 0.01$, and $^{***}P < 0.001$ relative to the indicated group.

data analysis. X. C. W.: Formal analysis. J. H. H.: Data curation. Y. Y. H.: Methodology. D. C.: Writing – review & editing. G. H.: Writing – review & editing. Y. Z. D.: Conceptualization. Z. W. Y.: Conceptualization, supervision, writing – review & editing.

Informed consent

Not applicable.

Ethics statement

The animal experiments were carried out following the guidelines of the Institutional Animal Care and Use Committee of Zhejiang University and were approved by the Institutional Animal Care and Use Committee of Zhejiang University. The assigned approval number is ZJU20250176.

Use of AI statement

During the preparation of this work, the authors used ChatGPT in order to correct grammatical issues. After using this tool, the authors reviewed and edited the content as needed and take full responsibility for the content of the publication.

References

[1] Falanga, V.; Isseroff, R. R.; Soulika, A. M.; Romanelli, M.; Margolis, D.; Kapp, S.; Granick, M.; Harding, K. Chronic wounds. *Nat. Rev. Dis. Primers* **2022**, *8*, 50.

[2] Li, R. T.; Liu, K.; Huang, X.; Li, D.; Ding, J. X.; Liu, B.; Chen, X. S. Bioactive materials promote wound healing through modulation of cell behaviors. *Adv. Sci.* **2022**, *9*, 2105152.

[3] Puca, V.; Marulli, R. Z.; Grande, R.; Vitale, I.; Niro, A.; Molinaro, G.;

Prezioso, S.; Muraro, R.; Di Giovanni, P. Microbial species isolated from infected wounds and antimicrobial resistance analysis: Data emerging from a three-years retrospective study. *Antibiotics* **2021**, *10*, 1162.

[4] Lu, M.; Wang, S.; Wang, T.; Hu, S. S.; Bhayana, B.; Ishii, M.; Kong, Y. F.; Cai, Y. C.; Dai, T. H.; Cui, W. G. et al. Bacteria-specific phototoxic reactions triggered by blue light and phytochemical carvacrol. *Sci. Transl. Med.* **2021**, *13*, eaba3571.

[5] Phan, S.; Feng, C. H.; Huang, R.; Lee, Z. X.; Moua, Y.; Phung, O. J.; Lenhard, J. R. Relative abundance and detection of Pseudomonas aeruginosa from chronic wound infections globally. *Microorganisms* **2023**, *11*, 1210.

[6] Uberoi, A.; McCready-Vangi, A.; Grice, E. A. The wound microbiota: Microbial mechanisms of impaired wound healing and infection. *Nat. Rev. Microbiol.* **2024**, *22*, 507–521.

[7] Pallavali, R. R.; Degati, V. L.; Lomada, D.; Reddy, M. C.; Durbaka, V. R. P. Isolation and *in vitro* evaluation of bacteriophages against MDR-bacterial isolates from septic wound infections. *PLoS One* **2017**, *12*, e0179245.

[8] Qin, S. G.; Xiao, W.; Zhou, C. M.; Pu, Q. Q.; Deng, X.; Lan, L. F.; Liang, H. H.; Song, X. R.; Wu, M. Pseudomonas aeruginosa: Pathogenesis, virulence factors, antibiotic resistance, interaction with host, technology advances and emerging therapeutics. *Signal Transduct. Target. Ther.* **2022**, *7*, 199.

[9] Huangfu, Y. N.; Li, S. Y.; Deng, L. D.; Zhang, J. H.; Huang, P. S.; Feng, Z. J.; Kong, D. L.; Wang, W. W.; Dong, A. J. Skin-adaptable, long-lasting moisture, and temperature-tolerant hydrogel dressings for accelerating burn wound healing without secondary damage. *ACS Appl. Mater. Interfaces* **2021**, *13*, 59695–59707.

[10] Z. F.; Huang, R. K.; Zheng, B. N.; Guo, W. T.; Li, C. K.; He, W. Y.; Wei, Y. Q.; Du, Y.; Wang, H. M.; Wu, D. C. et al. Highly stretchable, adhesive, biocompatible, and antibacterial hydrogel dressings for wound healing. *Adv. Sci.* **2021**, *8*, 2003627.

[11] Abbas, M.; Uçkay, I.; Lipsky, B. A. In diabetic foot infections antibiotics are to treat infection, not to heal wounds. *Expert Opin. Pharmacother.* **2015**, *16*, 821–832.

[12] Wang, Y.; Zhang, Y.; Yang, Y. P.; Jin, M. Y.; Huang, S.; Zhuang, Z. M.; Zhang, T.; Cao, L. L.; Lin, X. Y.; Chen, J. et al. Versatile dopamine-functionalized hyaluronic acid-recombinant human collagen hydrogel promoting diabetic wound healing via inflammation control and vascularization tissue regeneration. *Bioact. Mater.* **2024**, *35*, 330–345.

[13] Hong, Y. Y.; Wang, M. Y.; Hu, D. R.; Wang, Y. J.; Ji, S. F.; Xiang, J. B.; Zhang, H. L.; Chen, H. T.; Li, Y.; Xiong, M. C. et al. NIR-responsive multifunctional artificial skin for regenerative wound healing. *Adv. Funct. Mater.* **2024**, *34*, 2405876.

[14] Yang, M.; Sheng, L. L.; Zhang, T. R.; Li, Q. F. Stem cell therapy for lower extremity diabetic ulcers: Where do we stand. *Biomed. Res. Int.* **2013**, *2013*, 462179.

[15] Zhang, X. L.; Qu, Q. L.; Yang, A. Q.; Wang, J.; Cheng, W. X.; Deng, Y. K.; Zhou, A. Y.; Lu, T.; Xiong, R. H.; Huang, C. B. Chitosan enhanced the stability and antibiofilm activity of self-propelled prussian blue micromotor. *Carbohydr. Polym.* **2023**, *299*, 120134.

[16] Wang, Z. Y.; Du, B. W.; Gao, X. Y.; Huang, Y. L.; Li, M.; Yu, Z. H.; Li, J. Y.; Shi, X. Y.; Deng, Y.; Liang, K. N. Endogenous oxygen-evolving bio-catalytic fabrics with fortified photonic disinfection for invasive bacteria-caused refractory cutaneous regeneration. *Nano Today.* **2022**, *46*, 101595.

[17] Chen, J.; Liu, Y. J.; Cheng, G. P.; Guo, J. H.; Du, S.; Qiu, J. M.; Wang, C.; Li, C. C.; Yang, X. F.; Chen, T. K. et al. Tailored hydrogel delivering niobium carbide boosts ROS-scavenging and antimicrobial activities for diabetic wound healing. *Small* **2022**, *18*, 2201300.

[18] He, C. N.; Feng, P. P.; Hao, M. M.; Tang, Y.; Wu, X.; Cui, W. G.; Ma, J. Y.; Ke, C. H. Nanomaterials in antibacterial photodynamic therapy and antibacterial sonodynamic therapy. *Adv. Funct. Mater.* **2024**, *34*, 2402588.

[19] Liu, D.; Li, L.; Shi, B. L.; Shi, B.; Li, M. D.; Qiu, Y.; Zhao, D.; Shen, Q. D.; Zhu, Z. Z. Ultrasound-triggered piezocatalytic composite hydrogels for promoting bacterial-infected wound healing. *Bioact. Mater.* **2023**, *24*, 96–111.

[20] Zhao, P.; Zhang, Y.; Chen, X. A.; Xu, C.; Guo, J. Z.; Deng, M. G.; Qu, X. W.; Huang, P. S.; Feng, Z. J.; Zhang, J. M. Versatile hydrogel dressing with skin adaptiveness and mild photothermal antibacterial activity for methicillin-resistant Staphylococcus aureus-infected dynamic wound healing. *Adv. Sci.* **2023**, *10*, 2206585.

[21] Mao, C. Y.; Xiang, Y. M.; Liu, X. M.; Cui, Z. D.; Yang, X. J.; Yeung, K. W. K.; Pan, H. B.; Wang, X. B.; Chu, P. K.; Wu, S. L. Photo-inspired antibacterial activity and wound healing acceleration by hydrogel embedded with Ag/Ag@AgCl/ZnO nanostructures. *ACS Nano* **2017**, *11*, 9010–9021.

[22] Liu, Y. N.; Li, F.; Guo, Z. R.; Xiao, Y. Q.; Zhang, Y. L.; Sun, X. Y.; Zhe, T.; Cao, Y. Y.; Wang, L.; Lu, Q. Y. et al. Silver nanoparticle-embedded hydrogel as a photothermal platform for combating bacterial infections. *Chem. Eng. J.* **2020**, *382*, 122990.

[23] Liu, Z. W.; Zhao, X. Y.; Yu, B. R.; Zhao, N. N.; Zhang, C.; Xu, F. J. Rough carbon-iron oxide nanohybrids for near-infrared-II light-responsive synergistic antibacterial therapy. *ACS Nano* **2021**, *15*, 7482–7490.

[24] Liang, Y. P.; He, J. H.; Guo, B. L. Functional hydrogels as wound dressing to enhance wound healing. *ACS Nano* **2021**, *15*, 12687–12722.

[25] Zhang, J. Q.; Zhang, S. W.; Liu, C.; Lu, Z. T.; Li, M. F.; Hurren, C.; Wang, D. Photopolymerized multifunctional sodium alginate-based hydrogel for antibacterial and coagulation dressings. *Int. J. Biol. Macromol.* **2024**, *260*, 129428.

[26] Asadi, N.; Pazoki-Toroudi, H.; Del Bakhshayesh, A. R.; Akbarzadeh, A.; Davaran, S.; Annabi, N. Multifunctional hydrogels for wound healing: Special focus on biomacromolecular based hydrogels. *Int. J. Biol. Macromol.* **2021**, *170*, 728–750.

[27] Wang, R. M.; Mesfin, J. M.; Hunter, J.; Cattaneo, P.; Guimarães-Camboa, N.; Braden, R. L.; Luo, C.; Hill, R. C.; Dzieciatkowska, M.; Hansen, K. C. et al. Myocardial matrix hydrogel acts as a reactive oxygen species scavenger and supports a proliferative microenvironment for cardiomyocytes. *Acta Biomater.* **2022**, *152*, 47–59.

[28] Christman, K. L. Biomaterials for tissue repair. *Science.* **2019**, *363*, 340–341.

[29] Hu, J. J.; Altun, I.; Zhang, Z. F.; Albadawi, H.; Salomao, M. A.; Mayer, J. L.; Hemachandra, L. P. M. P.; Rehman, S.; Oklu, R. Bioactive-tissue-derived nanocomposite hydrogel for permanent arterial embolization and enhanced vascular healing. *Adv. Mater.* **2020**, *32*, 2002611.

[30] Seif-Naraghi, S. B.; Horn, D.; Schup-Magoffin, P. A.; Madani, M. M.; Christman, K. L. Patient-to-patient variability in autologous pericardial matrix scaffolds for cardiac repair. *J. Cardiovasc. Transl. Res.* **2011**, *4*, 545–556.

[31] Johnson, T. D.; DeQuach, J. A.; Gaetani, R.; Ungerleider, J.; Elhag, D.; Nigam, V.; Behfar, A.; Christman, K. L. Human *versus* porcine tissue sourcing for an injectable myocardial matrix hydrogel. *Biomater. Sci.* **2014**, *2*, 735–744.

[32] Traverse, J. H.; Henry, T. D.; Dib, N.; Patel, A. N.; Pepine, C.; Schaer, G. L.; DeQuach, J. A.; Kinsey, A. M.; Chamberlin, P.; Christman, K. L. First-in-man study of a cardiac extracellular matrix hydrogel in early and late myocardial infarction patients. *JACC Basic Transl. Sci.* **2019**, *4*, 659–669.

[33] Yamaoka, T.; Hoshiba, T. *Decellularized Extracellular Matrix: Characterization, Fabrication and Applications*; Royal Society of Chemistry: London, 2020; pp 116–138.

[34] Yang, P. C.; Kao, Y. C.; Lin, Y. P.; Chen, G. H.; Ho, C. H.; Liu, S. W.; Huang, S. C.; Lee, P. Y.; Chen, L. Y.; Huang, C. C.

Polydopamine nanoparticle-enhanced stem cell spheroid-derived decellularized extracellular matrix with antioxidant and tissue-adhesive properties for brain repair. *Biomaterials* **2026**, *324*, 123530.

[35] Su, J. J.; Lu, S.; Jiang, S. J.; Li, B.; Liu, B.; Sun, Q. N.; Li, J. J.; Wang, F.; Wei, Y. Engineered protein photo-thermal hydrogels for outstanding *in situ* tongue cancer therapy. *Adv. Mater.* **2021**, *33*, e2100619.

[36] Guo, Y. F.; Baschieri, A.; Mollica, F.; Valgimigli, L.; Cedrowski, J.; Litwinienko, G.; Amorati, R. Hydrogen atom transfer from HOO· to ortho-quinones explains the antioxidant activity of polydopamine. *Angew. Chem., Int. Ed.* **2021**, *60*, 15220–15224.

[37] Sun, C.; Yin, N. Y.; Wen, R. X.; Liu, W.; Jia, Y. X.; Hu, L. G.; Zhou, Q. F.; Jiang, G. B. Silver nanoparticles induced neurotoxicity through oxidative stress in rat cerebral astrocytes is distinct from the effects of silver ions. *NeuroToxicology* **2016**, *52*, 210–221.

[38] Fu, Y.; Yang, L.; Zhang, J. H.; Hu, J. F.; Duan, G. G.; Liu, X. H.; Li, Y. W.; Gu, Z. P. Polydopamine antibacterial materials. *Mater. Horiz.* **2021**, *8*, 1618–1633.

[39] Yu, Y. L.; Li, P. F.; Zhu, C. L.; Ning, N.; Zhang, S. Y.; Vancso, G. J. Multifunctional and recyclable photothermally responsive cryogels as efficient platforms for wound healing. *Adv. Funct. Mater.* **2019**, *29*, 1904402.

[40] Wu, Y. Z.; Liao, Q.; Wu, L.; Luo, Y. X.; Zhang, W.; Guan, M.; Pan, H. B.; Tong, L. P.; Chu, P. K.; Wang, H. Y. ZnL_2-BPS integrated bone scaffold under sequential photothermal mediation: A win-win strategy delivering antibacterial therapy and fostering osteogenesis thereafter. *ACS Nano* **2021**, *15*, 17854–17869.

[41] Poirel, L.; Jayol, A.; Nordmann, P. Polymyxins: Antibacterial activity, susceptibility testing, and resistance mechanisms encoded by plasmids or chromosomes. *Clin. Microbiol. Rev.* **2017**, *30*, 557–596.

[42] Huo, J. J.; Jia, Q. Y.; Huang, H.; Zhang, J.; Li, P.; Dong, X. C.; Huang, W. Emerging photothermal-derived multimodal synergistic therapy in combating bacterial infections. *Chem. Soc. Rev.* **2021**, *50*, 8762–8789.

[43] Qing, Y.; Cheng, L.; Li, R. Y.; Liu, G. C.; Zhang, Y. B.; Tang, X. F.; Wang, J. C.; Liu, H.; Qin, Y. G. Potential antibacterial mechanism of silver nanoparticles and the optimization of orthopedic implants by advanced modification technologies. *Int. J. Nanomedicine* **2018**, *13*, 3311–3327.

[44] He, J. H., Shi, M. T., Liang, Y. P., Guo, B. L. Conductive adhesive self-healing nanocomposite hydrogel wound dressing for photothermal therapy of infected full-thickness skin wounds. *Chem. Eng. J.* **2020**, *394*, 124888